

In-flight Performance and Calibration of the Chandra High Resolution Camera Imager (HRC-I)

A. Kenter, J.H. Chappell, R. Kraft, G. Meehan, S.S. Murray, M. Zombeck, K.T. Hole, M. Juda, R.H. Donnelly,
D. Patnaude, D. Pease, C. Wilton, P. Zhao, G. Austin

Smithsonian Astrophysical Observatory, 60 Garden St., Cambridge, MA 02138

G. Fraser, J. Pearson, J. Lees, A. Brunton
University of Leicester, Leicester, LE1 7RH, England

M. Barbera, A. Collura, S. Serio
Osservatorio Astronomico G.S. Vaiana, I-90134 Palermo, Italy

ABSTRACT

The High Resolution Camera (HRC) is one of the two focal plane instruments on the NASA Chandra X-ray Observatory (CXO) which was successfully launched on July 23, 1999. The CXO performs high resolution spectroscopy and imaging in the X-ray band of 0.07 to 10 keV. The HRC instrument consists of two detectors, HRC-I for imaging and HRC-S for spectroscopy. The other focal plane instrument is the Chandra CCD Imaging Spectrometer (ACIS).

Each HRC detector consists of a thin aluminized polyimide window, a chevron pair of microchannel plates (MCPs) and a crossed grid charge readout. The HRC-I is an $\sim 100 \times 100$ mm detector optimized for high resolution imaging and timing, the HRC-S is an $\sim 20 \times 300$ mm detector optimized to function as the readout for the Low Energy Transmission Grating (LETG).

In this paper we present and compare flight results with the latest results of the ground calibration for the HRC-I detector. In particular we will compare ground and in flight data on detector background, effective area, quantum efficiency and point spread response function.

The development of the HRC is a collaborative effort between The Smithsonian Astrophysical Observatory, University of Leicester UK and the Osservatorio Astronomico, G.S. Vaiana, Palermo Italy.

Keywords: Chandra, AXAF, High Resolution Camera.

1 INTRODUCTION

The Chandra X-ray Observatory is a major space observatory designed to perform high resolution imaging and spectroscopic observations in the 0.07 to 10 keV X-ray energy band. The major observatory components are the High Resolution Mirror Assembly (HRMA), two sets of objective transmission gratings and the two focal plane instruments. The HRMA consists of four pairs of nested iridium coated Wolter type I optics. The HRMA has a ~ 10 meter focal length and a plate scale of $49\mu\text{m}$ per arcsec. The objective transmission gratings consist of the Low Energy Transmission Gratings (LETG) and the High Energy Transmission Gratings (HETG). The two focal plane instruments are the AXAF CCD Imaging Spectrometer (ACIS) and the High Resolution Camera (HRC).

The HRC consists of two Microchannel Plate (MCP) based detectors; one for high resolution large field of view imaging and a second detector which is optimized as the readout for the LETG. The HRC detectors have spatial resolutions of < 0.5 arcsec and limited inherent non-dispersive energy resolution of $\frac{E}{\Delta E} \approx 1$.

More in depth discussions of the Chandra mission, spacecraft, other instruments and subsystems are presented

elsewhere.^{1,2,3,4} Papers discussing the HRC-S detector in-flight calibration can be found elsewhere in these proceedings.^{5,6}

2 THE HIGH RESOLUTION CAMERA (HRC)

The HRC detectors are technological descendants of the highly successful Einstein and ROSAT High Resolution Imagers (HRIs).^{7,8} The HRC detectors differ from their predecessors primarily in size, geometry and electronic implementation. In addition, the HRC detectors use MCPs fabricated from low radioactive content glass and the HRC instrument employs an active cosmic ray anti-coincidence shield.

The HRC instrument consists of two detectors; the HRC-I and the HRC-S. Both detectors have excellent spatial resolution ($\sim 20\mu\text{m}$ FWHM)⁹, and fast event-time-tagging ($16\mu\text{s}$). The HRC detectors use MCPs coated with a CsI photocathode and thin aluminized polyimide filters to provide high detector quantum efficiency at the low energies of the Chandra energy band where the effective HRMA area is largest, and low sensitivity to UV and visible light. The HRC-I is intended for low background, large Field-of-View (FOV) high resolution imaging and timing. The HRC-I has a geometrical area of $93\text{mm} \times 93\text{mm}$. In combination with the HRMA focal length of 10m, this provides a field of view of $\sim 31 \times 31$ arcmin. The combination of low background, large FOV, high angular resolution and precise timing ensures that the HRC-I has unprecedented performance as a soft X-ray faint object camera. The HRC-S is optimized to act as the readout for the LETGs. More in-depth descriptions of the HRC-S and its use for the LETG readout can be found elsewhere.^{4,10,11}

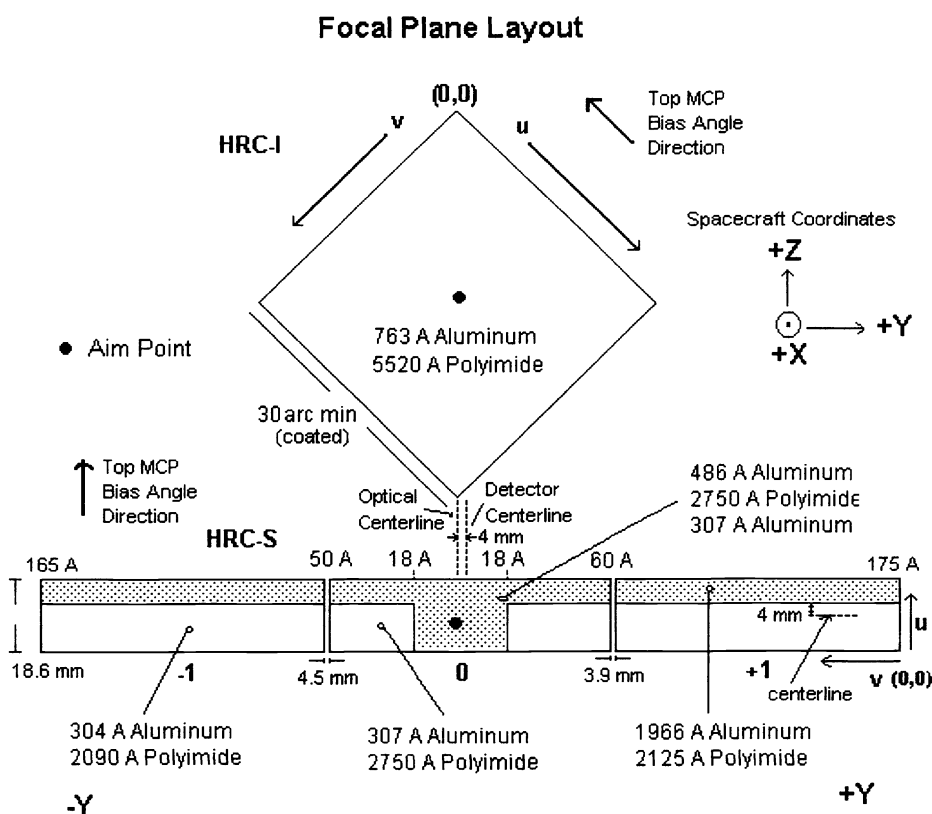


Figure 1: Focal plane layout of the HRC showing the HRC-I and HRC-S.

The HRC-I detector consists of an aluminized polyimide UV/Ion Shield (UVIS); a CsI photocathode chevron pair of MCPs and a Crossed Grid Charge Detector (CGCD) readout. The CsI photocathode is deposited on the input face of front MCP. The HRC instrument also employs passive and active shielding to reduce its background event rate. A schematic representation of the HRC-I components is presented in Figure 2. The UVIS blocks out-of-band ultraviolet and visible photons and low energy ions and electrons. The CsI enhances photoelectric conversion of the X-ray photon. The two MCPs in the chevron arrangement provide electron multiplication of $\sim 2 \times 10^7$ while minimizing ion feedback. The CGCD collects the resulting electron cloud, from which the electronics determine the pulse height amplitude, arrival time, and position of the X-ray photon.

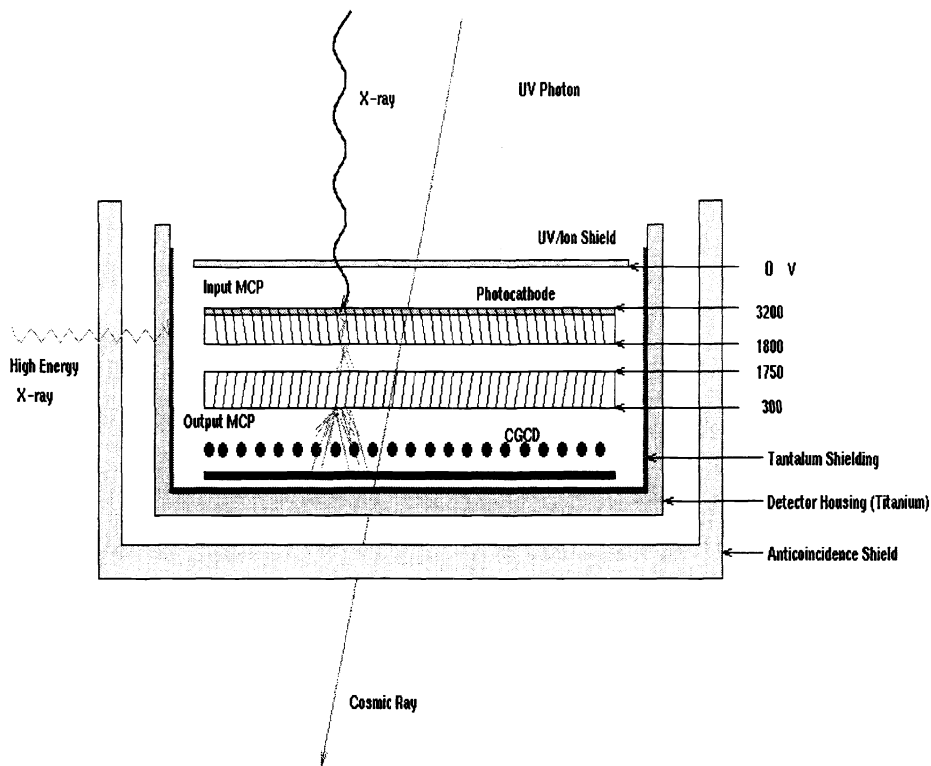


Figure 2: Schematic representation of HRC type detectors showing UV ion shield, photocathode, chevron pair of MCPs Crossed Grid Charge Detector (CGCD) readout and shielding.

2.1 The UV/Ion Shields

The UVIS for the HRC detectors consists of an aluminized thin plastic membrane. For the HRC-I detector, the UVIS consists of $\sim 800\text{\AA}$ aluminum vacuum deposited on $\sim 5500\text{\AA}$ polyimide film. The UVIS was manufactured by the Luxel Corporation of Friday Harbor Washington.

The function of the UV ion shield is multifold: it blocks the sensitive photocathode from seeing out-of-band ultra-violet and visible light; it shields the detector from low energy electrons and ions, and it provides a well defined electric field above the input MCP. A more detailed description of the UVIS function, tests, and of the HRC UV ion shield calibration, have been presented elsewhere^{12,13,14}.

2.2 Photocathode

To enhance the detector quantum efficiency a $\sim 14000\text{\AA}$ CsI photocathode was vacuum deposited on to the input face of the top MCP. The resulting photocathode enhances quantum efficiency; however, it is susceptible to damage from exposure to humid air. Before and during launch, the HRC MCPs were continually under vacuum or in a dry nitrogen atmosphere.

2.3 Microchannel Plates

The HRC-I MCPs are 1.2mm thick and are 100mm \times 100mm square. They have $10\mu\text{m}$ pores on $12\mu\text{m}$ centers. Both the top and bottom MCPs were sliced to give the pores a nominal 6° bias angle. The pair are assembled with their pore angles in a chevron configuration to minimize ion feedback. The bias angle introduces an azimuthal asymmetry in quantum efficiency for non-normal incidence illumination. However for a 6° bias, this asymmetry maximizes the overall detector efficiency when it is averaged over energy and the incident cone angles from the HRMA. The HRC-I MCPs were manufactured by the Galileo Electro Optics Corporation (GEOC; now Burle) in Sturbridge, MA. These MCPs are manufactured from a proprietary low internal radioactivity glass.

2.4 The Crossed Grid Charge Detector

The electron charge cloud exiting the rear of the output MCP is collected by two orthogonal grids of gold alloy wires. These wires are separated and held in place by a laser-ruled alumina ceramic block. Beneath the two planes of wires is a deposited gold reflector plane which is biased to ensure $\approx 100\%$ collection of the charge cloud. The grid wires are nominal $100\mu\text{m}$ diameter on $200\mu\text{m}$ spacing. Each wire is connected to its nearest neighbor with a $10\text{ k}\Omega$ resistor. Every eighth wire is then connected to a charge sensitive amplifier. There are 64 amplifiers or “taps” for each axis. The output face of the rear MCP is attached to a separate “MCP trigger” charge amplifier. This “MCP trigger” amplifier senses the exit of the charge cloud and initiates the on-board electronics which then process an event.

2.5 Event Processing

2.5.1 “Three Tap” Algorithm

The X-ray position is determined by calculating the centroid of the charge cloud exiting the rear MCP via the “three tap” algorithm. In short, the three tap algorithm determines the charge cloud centroid using a combination of digital and analog electronics and off-line processing. Fast discriminators and logic circuits first determine a “coarse” position, which is the amplifier with maximum detected charge. Analog switches then select the three amplifiers centered on that coarse position and steer them to analog to digital converters. The coarse position and three digitized values are telemetered and then used off-line on the ground to calculate the event position. This process is performed for each axis. The reconstructed X-ray position can then be written as the sum of a coarse position and a charge centroid term centered on the coarse position:

$$pos = cp_i + \left(\frac{Q_{cp_{i+1}} - Q_{cp_{i-1}}}{Q_{cp_{i-1}} + Q_{cp_i} + Q_{cp_{i+1}}} \right) \times \Delta \quad (1)$$

where cp is the coarse position, $Q_{cp_{i+1}}$ is the charge measured on the cp_{i+1} tap, and Δ is the distance between taps. Since the charge cloud extends beyond the two outer taps, each of the outer amplifiers underestimates the amount charge needed to calculate the true centroid. For an event perfectly centered on the middle tap, the

charge loss beyond the outer two taps is symmetric and cancels. If however, the event position is not over the center of a tap, the fractional error due to the charge loss in the two surrounding taps is different and produces a small systematic error in the reconstructed position. The small systematic positional error combined with the coarse position logic produce “gaps” in the HRC images. These gaps are perfectly aligned with the detector axes and correspond to positions exactly half-way between amplifier taps. Since the gaps are systematic, they can and are removed.

2.6 Modified “Three Tap” Algorithm

The spatial distribution of the charge cloud leaving the rear of the 2nd MCP has a very specific shape for X-ray induced events. This shape has often been modeled as the combination of a Gaussian and a Lorentzian distribution.¹⁵ Due to this specific shape, it has been observed and simulated via Monte Carlo techniques that the fine position term:

$$\left(\frac{Q_{cp_{i+1}} - Q_{cp_{i-1}}}{Q_{cp_{i-1}} + Q_{cp_i} + Q_{cp_{i+1}}} \right) \quad (2)$$

and the complementary term:

$$\left(\frac{Q_{cp_i}}{Q_{cp_{i-1}} + Q_{cp_i} + Q_{cp_{i+1}}} \right) \quad (3)$$

are highly correlated, in fact the shape of a scatter plot of the two quantities for X-ray induced events closely describes a hyperbola. A scatter plot of the two quantities is presented in Figure 3. Non X-ray events, primarily those due to the passage of charged particles, produce charge distributions that are often larger, and are spatially extended and complex. As such, it is possible to remove many non X-ray background events by screening those events that do not fit the hyperbola. Furthermore, since the charge distribution is centrally peaked, the complement Q_{cp_i} term is larger and less susceptible to noise induced errors than the $Q_{cp_{i+1}} - Q_{cp_{i-1}}$ difference term. It is therefore possible to use the complement term, and the best fit hyperbolic locus to correct those events where instrumental noise has compromised the three-tap fine position. Results from this modified three-tap algorithm, or “hyperbolic” filter for background reduction and imaging performance are presented in the background and PSF sections of this paper. A much more detailed explanation of this technique will be presented in a future publication.

3 HRC-I IN-FLIGHT PERFORMANCE

The following sections will present the flight performance of the HRC-I detector in comparison with preflight expectations and models. The three main sections to be addressed are: background rates, effective area and point spread function (PSF).

3.1 Background and Shielding

The intrinsic HRC-I background counting rate has been minimized by constructing the HRC detectors of materials with low radioactive content. In particular, MCPs fabricated from glass without potassium or rubidium have resulted in background reductions > 10 over previous MCP glass formulations. The best laboratory measurements incorporating external shielding with HRC-I type MCPs have achieved counting rates of as low as $0.04 \text{ cts s}^{-1} \text{ cm}^{-2}$ (Kenter *et. al.* 1995)¹⁶; this contribution would correspond to $\sim 1 \times 10^{-6} \text{ s}^{-1} \text{ arcsec}^{-2}$ in the HRMA/HRC-I focal plane.

In-flight background of the HRC detectors is due to charged particles, the diffuse X-ray background and out-of

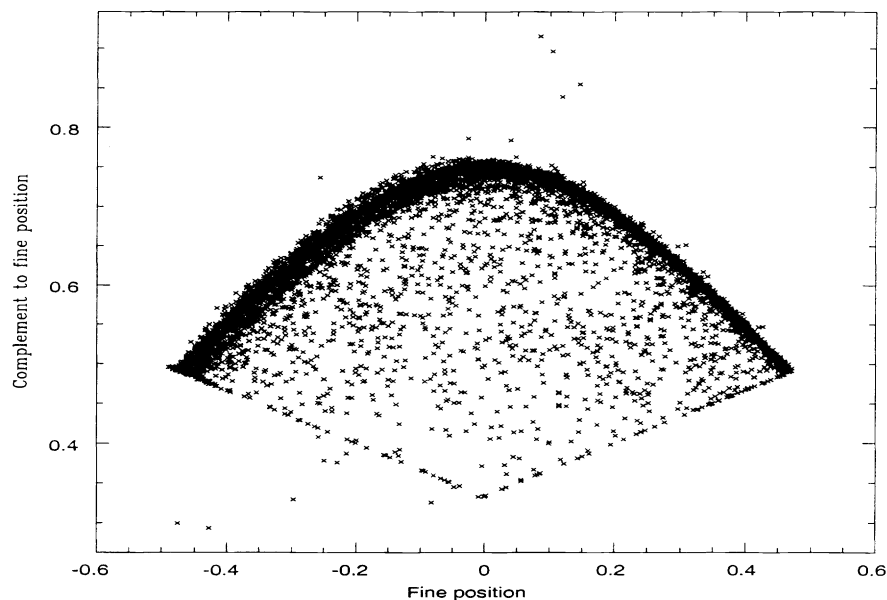


Figure 3: Distribution showing the correlation between the fine position term of the 3-tap algorithm and the complement to the fine position term. X-ray events are preferentially distributed along a hyperbola. Particle induced events and misprocessed events are distributed off the hyperbolic locus. Larger spread for fine position < 0 is due to electronic noise (see text).

band high energy ($> 20 \text{ keV}$) photons. Potentially the largest component of the HRC background is due to minimum ionizing primary cosmic rays. These cosmic rays can register as events in the HRC detectors.

To eliminate the background component due to these minimally ionizing cosmic rays the HRC instrument incorporates a plastic scintillator based anti-coincidence detector. Details of the anti-coincidence detector shield have been presented elsewhere⁹. The anti-coincidence detector provides 4π Steradian coverage and rejects events which register in the HRC and the shield within a narrow coincidence time window ($\sim 1\mu \text{ sec}$). In flight counting rates for the anti-coincidence shield are typically $\sim 4500 \text{ cts s}^{-1}$. For this rate, the effective QE of the HRC-I detector is reduced by an absolute 0.45% due to accidental coincidences. The anti-coincidence shield reduces the onboard HRC-I detector background counting rate from $\sim 250 \text{ cts s}^{-1}$ to $\sim 30 - 40 \text{ cts s}^{-1}$. Of the remaining $\sim 30 \text{ cts s}^{-1}$ background it is estimated that $\sim 3 \text{ cts s}^{-1}$ is due to the diffuse X-ray background, $\sim 5 - 10 \text{ cts s}^{-1}$ is due to intrinsic detector background and the remaining $\sim 20 \text{ cts s}^{-1}$ is of indeterminate origin. It is hypothesized that some of this residual $\sim 20 \text{ cts s}^{-1}$ could be inefficiencies in the anti-coincidence shield, charged particles focused by the HRMA, or radio-activation of detector elements.

Since the MCPs have a non-negligible detection efficiency for high ($> 20 \text{ keV}$) energy photons¹⁶, tantalum shielding has been placed around the HRC instrument. Detailed shielding models taking into account spallation and transport within the Chandra space craft have been presented elsewhere¹⁷.

As has been previously discussed, the modified three-tap off-line software event processing further reduces the background counting rate to $< 30 \text{ cts s}^{-1}$. The result of this HRC event processing on background and X-rays is presented in Figure 4. The HRC hyperbolic locus test reduces background by approximately 40% while X-ray events are reduced only approximately 5%.

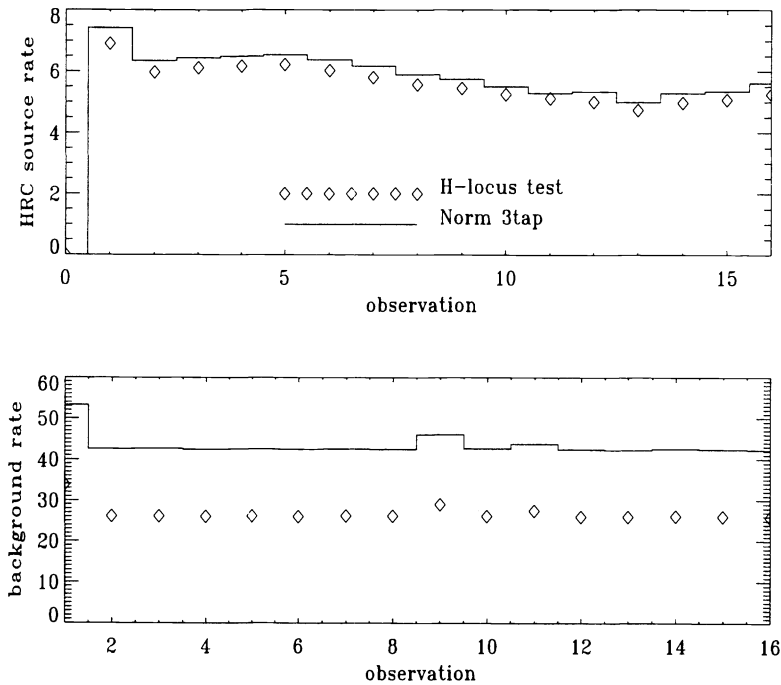


Figure 4: Results of modified 3-tap positioning algorithm (hyperbolic test) on a series of X-ray and background observations of the RS CVn star AR Lac. Average background reduction for these observations is 39%. Source x-rays are reduced by only 5%.

In flight performance of the various background reduction techniques are presented in Figure 4 and Figure 5. Figure 5 also shows that detector background is variable and occasionally shows burst of increased rate. Analysis of these bursts show that they are distributed uniformly over the HRC-I detector.

With all background reduction techniques employed, the overall, spatially averaged quiescent background for the HRC-I detector is $\approx 1 \times 10^{-5} \text{cts s}^{-1} \text{arcsec}^{-2}$.

The spatial distribution of the HRC-I background has been mapped out using several different techniques with different data sets. The removal of point and extended sources from HRC images presents a complex task as most observations have a relatively bright source in the center of the HRC field of view. Removing the source and the wings of the HRMA PSF is problematic since the background is low and even a small scattered component from the PSF can influence what is thought to be the background. A preliminary background map is presented in Figure 6. The background map shows a broad trend of $\sim 10\%$ increase in background across the diagonal of the HRC-I detector. The map is aligned to correspond with Figure 1. This particular map is from a 10 ksec observation with no source in the center of the FOV. Background maps from much longer observations and ensembles of observations are presently being analyzed.

The High Resolution Imager (HRI) on ROSAT suffered from a “UV leak” or unexpected sensitivity to ultraviolet radiation.¹⁸ This sensitivity was demonstrated early in the ROSAT mission with the detection of the 0 magnitude star Vega (alpha Lyr; A0V; U=0.02, B= 0.03, V= 0.03; alpha(2000) = 18h 36m 56.2s , dec(2000) = +38° 47' 01”) by the HRI with a count rate of 0.1cts s^{-1} . This unexpected sensitivity was the result of the higher than predicted UV transmission of the HRI’s aluminized Lexan UV/Ion shield. During the design stage

of the HRC-I, we developed a more UV opaque UV/Ion shield by replacing the Lexan substrate with polyimide; this was accomplished without compromising the X-ray transmission. An observation of Vega with the HRC-I to verify the low UV response yielded an upper limit for the count rate of Vega of $1 \times 10^{-3} \text{cts s}^{-1}$. The predicted count rate calculated by multiplying Vega's spectrum by the HRC-I effective area in the UV and visible spectral bands (see Figure 7) is $7 \times 10^{-4} \text{cts s}^{-1}$. Since the collecting area of ROSAT and Chandra mirrors are about the same in the UV, we have reduced the HRC-I sensitivity to Vega by a factor of about 100 over that of the ROSAT HRI by using polyimide instead of Lexan. Based upon these observations, the UV/Ion shields are performing as designed. We will observe additional stars in future calibration activities in order to further verify the out-of-band response of the HRC.

3.2 Effective Area

The measured effective area (EA) of the HRC-I/HRMA is the ratio of the HRC-I count rate to the input X-ray flux density at the HRMA aperture as a function of energy. The EA can be modeled from sub assembly calibrations as the product of the HRMA effective area, the UVIS transmission and the CsI coated MCP efficiency. The subassembly models are presented in Figure 8. Structure in the HRC-I/HRMA EA is therefore evident at energies of the iridium, carbon, cesium and iodine edges. Both the UVIS and the HRMA have been measured and modeled extensively and are known with little relative uncertainty. Details of the UVIS measurements and modeling are presented elsewhere^{13,14}. Similarly, the HRMA calibration has been described in detail and is presented in Van Speybrock *et al.* 1997¹⁹ and references contained there-in. Of the three sub-assembly components in the EA, the least well known is the quantum efficiency of the CsI coated MCPs. We will now specifically present the procedure that was used to determine the QE of the HRC-I MCPs.

To model the MCP QE over the entire Chandra energy band, the coated MCP quantum efficiency was determined at a discrete number of energies. The efficiency was then interpolated to a finer energy scale using a physical model that depends on the 1993 Henke mass absorption coefficients²⁰.

3.2.1 Quantum Efficiency

The quantum efficiency of the HRC-I was determined as a function of energy and position by combining data from three distinct data sets: These data sets were: pre-flight on axis effective area measurements, SAO HRC-I flat field (FF) illumination tests and synchrotron data measurements of non-flight coated MCP detectors.

The effective area of the HRMA/HRC-I was measured on the ground at the X-Ray Calibration Facility (XRCF) at the Marshall Space Flight Center (MSFC). Details of these measurements and of the XRCF calibration facility are discussed in D.Patnaude *et al.*²¹ 1998 and in J.Kolodziejczak *et al.*,²² 1995.

Using these XRCF determined EA measurements, MCP QE values were determined by dividing out the XRCF appropriate HRMA effective mirror area and the transmission of the UVIS. Only on-axis EA measurements were used. In addition to the HRMA effective area, the effects of the HRMA cone angles on MCP QE values had to be taken into account. The HRMA cone angle correction for the HRC-I is presented in Figure 14; it differs significantly from 1.0 (normal incidence) only for energies $< 500 \text{ eV}$ for the HRC-I. These HRMA angle corrections are the result of an elaborate experimental campaign to measure and model the dependence of coated MCP quantum efficiency on MCP pore angle, X-ray incidence angle, and X-ray energy. Details of these measurements are presented in (Kenter *et al.*,1997).²³

The SAO flat field illumination tests were performed on the HRC-I detector in its final flight configuration. These flat field tests measured the QE of the HRC-I detector with X-rays at approximately normal incidence to the MCP surface. These measurements will be discussed in detail in the following section.

The synchrotron data were obtained at the Daresbury Synchrotron using non-flight, HRC-S type MCPs in non-flight like detectors, with non-flight like electronics. These “representative” detectors were coated with CsI at the University of Leicester. In contrast the HRC-I flight MCPs were manufactured by the Galileo Electro Optics Corporation (now Burle) and were coated with CsI at SAO. The synchrotron data measured the QE of the MCP detectors near the Cs and I *M* edges and between 277 and 350 eV. No cross calibration of these representative MCPs were done with the HRC-I detector. Due to the different heritage and the lack of cross-calibration, there may be large systematic errors introduced by incorporating these data into the HRC-I instrument calibration. The synchrotron data were also obtained at “normal incidence”.

The method for determining the QE of the HRC-I detector is to first derive the QE of the CsI coated MCPs without the UVIS at a set number of energies for normal incidence illumination; this entails dividing out the transmission of the UVIS and dividing out the HRMA effective area, and HRMA cone angle dependence from the HRC-I/HRMA EA measurements. These discrete MCP QE values are combined with an interpolation scheme to determine the QE versus energy for the CsI coated MCPs on a finer energy scale. The synchrotron QE data near the Cs and I *M* edges is then scaled appropriately and spliced into MCP QE versus energy data. The QE of the overall HRC-I detector is then obtained by multiplying the MCP QE by the HRC-I UVIS transmission. The appropriate corrections for the HRMA cone angles are then applied. The net result is a continuous model of HRC-I quantum efficiency over the Chandra energy band which is appropriate for the converging beam of the HRMA. The following subsections will describe the individual data sets and the interpolation technique. The final step combines the interpolated model with the HRMA effective area to produce the HRC-I/HRMA effective area .

3.2.2 XRCF Measurements

The X-ray sources used at XRCF were an Electron Impact Source (EIPS) with various anodes and filters; a Rotating Anode Source (RAS) with either a High Resolution Erect Field Spectrometer (HIREFS) (used as a monochromator) or a Double Crystal Monochromator (DCM).

The HIREFS source was intended to provide EA measurements for energies from 400 to 2000 eV. In practice, the HIREFS data suffered from large spatial non-uniformities over the input face of the HRMA. Furthermore, the HIREFS suffered from higher-order spectral contamination of the continuum source and from strong spectral contamination by tungsten *M* lines near 1.7 keV. The poor spectral quality of the HIREFS data and the low energy resolution of the HRC-I detector necessitated a complex “boot-strapping” process to extract HRC-I/HRMA EA values. The ensuing large systematic errors made the HIREFS data useful only for qualitative comparison with other data. HIREFS determined EA data were not used to determine the here-in presented HRC-I QE.

The DCM data comprises the largest and best XRCF data set; it had little higher order contamination and the X-ray beam was relatively uniform over the aperture of the HRMA. The DCM data, however, were limited to $E > \sim 2$ keV. All DCM measurements through 7keV were incorporated into the QE model. The QE was then extrapolated out to 10 keV from the 6.3 keV and 7 keV DCM measurements based on trends in synchrotron measurements. DCM measurements for $E > 7keV$ were inconsistent and were omitted.

Only one EIPS XRCF EA measurement at 277 eV was used for the HRC-I QE calibration. Other measurements at 183 eV were not consistent and have been left out.

3.2.3 SAO Flat Field QE Measurements

Following the XRCF calibration the HRC instrument returned to SAO for modification and flat-field illumination tests. The purpose of the flat field illuminations were to determine the average and spatially dependent QE of the HRC-I detector.

During flat field testing, the HRC instrument was mounted to an ~ 7 meter X-ray pipe to provide approximately normal incidence X-ray illumination. A series of adapter flanges were used to mount the instrument externally to the vacuum chamber and to illuminate the HRC-I and each of the HRC-S segments separately. This mounting scheme allowed access to the HRC electronics for testing and modification during operation. X-ray illumination was provided by a Manson Model 5 multi-anode electron impact source. The anodes and filter combinations listed in Table 1 were used. The SAO Flat Field facility is depicted in Figure 9. The absolute beam intensity

Line	Energy	Filter	MFPs	V_A	L/C
B $K\alpha$	183 eV	7 μ parylene-C	5.87	600 V	48.4
C $K\alpha$	277 eV	33 μ polypropylene	5.94	1000 V	171
O $K\alpha$	525 eV	2 μ Cr	4.67	1000 V	29.3
Ni $L\alpha$	851 eV	2 μ Cu	3.80	2500 V	2.55
Al $K\alpha$	1487 eV	50 μ Al	5.40	4000 V	38.9
Ag $K\alpha$	2984 eV	10 μ Ag	4.86	6000 V	0.60
Ti $K\alpha$	4511 eV	150 μ Ti	6.80	10000 V	6.73
Fe $K\alpha$	6404 eV	125 μ Fe	6.97	10000 V	1.78

Table 1: Summary of line energies, filters, thicknesses, anode voltages, and predicted line-to-continuum ratio of the X-ray source for HRC-I flat fields.

at the input of the HRC was measured using a Manson Model 04 flow proportional counter which was mounted on a retractable arm. This Beam Normalization Detector (BND) was not operated concurrently with the HRC as it had a slow gas leak through its window which spoiled the vacuum too close to the input face of the MCPs. Absolute flux measurements and temporal monitoring were performed by first cross calibrating a second Manson model 04 Monitor Detector (MD) flow proportional to the BND. This MD was close to the actual X-ray source and operated concurrently with the HRC detectors. By using the MD rates and the MD to BND cross-calibration the QE of the HRC detector was measured. The QE of the HRC was calculated as:

$$QE_{hrc} = \frac{R_{hrc}}{I_{hrc}\Omega_{hrc}} \quad (4)$$

Where:

$$I_{hrc} = \frac{R_{MD}}{QE_{BND}\Omega_{BND}} \times \left(\frac{BND}{MD}\right)_{cc} \quad (5)$$

and $\left(\frac{BND}{MD}\right)_{cc}$ is the BND to MD cross calibration ratio. The QE of the proportional counters were calculated from their window properties and mechanical dimensions; no cross calibration to any standards were performed. The window transmission of the BND and MD proportional counters were measured extensively using a McPherson Monochromator and subsequently modeled at SAO. The effective counter depth provided by the manufacturer was used. Gas pressure, composition (CH_4 or $P10$) and temperature were controlled and/or measured throughout the tests. The HRC-I was illuminated for a set time to insure that at least 10^7 events were collected for all the anodes excepting boron, where only $\sim 3 \times 10^6$ events were collected.

During the Flat Field illumination tests of the HRC detectors, the electronics were modified so as to allow a data rate $\approx 10\times$ the telemetry limit of ≈ 184 events s^{-1} . In practice, data rates were intentionally limited to

1200 – 1400 events s^{-1} for the HRC-I for all energies except for boron; the boron data were flux limited. The $10\times$ operation of the HRC necessitated that dead-time corrections be applied to the flat field QE values. The dead time for the HRC detectors has been independently measured to be $\tau = 68.5\mu s$; the majority of this is due to an ADC conversion time. Dead time corrections can be applied to the flat field HRC QE values by considering the instrument as a non-paralyzable (non-extendible dead time) detector with a characteristic dead time of $\tau = 68.5\mu s$. Using just the measured rates of $R_{meas} \sim 1200cts s^{-1}$, without correction would cause an underestimate of the true QE, by $\sim 9\%$. It can be easily shown under the above assumptions that:

$$\frac{QE_{true}}{QE_{meas}} = \frac{R_{true}}{R_{meas}} = \frac{1}{1 - R_{meas}\tau} \quad (6)$$

Where the true QE values are the “zero-rate” limits.

The QE values as quoted are averaged over the entire photocathode coated HRC-I MCP area. The line to continuum ratios as listed in Table 2 are based on theoretical modeling of the bremsstrahlung and line emission as modified by the X-ray filter. Several of the flat field QE points were suspect when compared with QE measurements from XRCF data. The Ag L_{α} line, which had a very low line to continuum ratio and an anomalously low QE measurement, was rejected from further consideration. The Ti K value as quoted is actually a mixture of the the K_{α} and K_{β} lines where the normal $K_{\beta}:K_{\alpha}$ ratio is increased by the effect of the $125\mu m$ Ti filter ($\times \sim 1.5$). The enhanced ratio and the fact that the two Ti lines straddle a significant photocathode edge (I L_{III} edge at 4550 eV) caused a significant overestimate of the Flat Field QE HRC at 4510 eV. This FF QE measurement was excluded from the calibration.

The Fe anode-Fe filter combination also enhanced the $K_{\beta}:K_{\alpha}$ ratio however it did not fall near any detector feature. The QE at Fe K as determined from the flat field illumination was $\sim 5\%$ lower than XRCF data in the same energy region. No systematic errors could account for this discrepancy. The Fe flat field point was also left out as input to the QE model. The high $K_{\beta}:K_{\alpha}$ ratios for the Ti and Fe anodes were confirmed using an X-ray CCD camera.

HRC-I QE		
Element	Energy (eV)	QE
B	183	0.062
C	277	0.20
O	525	0.12
Ni	851	0.27
Al	1487	0.31
Ag	2980	0.093
Ti	4511	0.10
Fe	6404	0.14

Table 2: Table of Flat Field (normal incidence) HRC-I QE values (with UVIS) corrected for dead time. Values are averaged over the CsI coated region of the HRC-I detector.

3.2.4 Synchrotron Measurements

A series of measurements were performed on CsI coated MCPs at the Daresbury synchrotron. The purpose of these measurement was to measure the absolute and relative QE of MCPs over the Chandra energy band. Special emphasis was placed on sampling near the various detector features such as the absorption edges of Cs and I. The CsI photocathode coatings were applied at the University of Leicester to MCPs produced by Photonis SAS, formerly Philips Photonics whereas the actual HRC coatings were applied at SAO. The

representative MCPs were then incorporated into detectors and tested at the Daresbury synchrotron which was operated in low current mode to allow operation of the detectors in single photon counting mode. The various Daresbury calibration campaigns are discussed in detail elsewhere^{24,25}.

Two subsets of the synchrotron data were incorporated as input to the HRC QE calibration. The first set of data was collected in January 1995 at beam line 6.1 of the Daresbury Synchrotron. These data spanned the energy band of 250-350eV in 1eV steps using a 1200 line-per-mm Miyake plane grating monochromator. The spectrum of the monochromator and associated optics had been measured previously using a tungsten grid reference detector. High rates in the MCP detector necessitated that the data be corrected for dead time and gain suppression. Following the synchrotron measurements, the relative QE versus energy data were normalized to a laboratory measurement of QE at carbon *K* (277eV) at the University of Leicester. This data was then again normalized to the Flat Field QE value at 277eV.

The second set of Daresbury Synchrotron data was collected in October 1997 on beam-line 1.1. This data spanned the energy band of ~ 450 to 800eV in 0.5 eV steps using a Ni(3) grating and used a flow proportional counter for absolute normalization of the beam. Unfortunately, the input flux was spoiled by carbon contamination of the beam-line optics and higher order carbon and oxygen spectral contamination. Details of this second data set are discussed in detail by Rideout *et. al.*, 1998²⁵.

3.2.5 MCP QE Model—Interpolation to a Finer Energy Scale

The QE of the CsI coated HRC-I MCPs was interpolated to a finer energy grid using: three sets of input points. These input points were: the flat field QE measurements, QE values obtained from XRCF EA measurements and the synchrotron data from 277 through 350 eV.

The interpolation scheme is outlined in Juda, M. 1997²⁶ and is based on earlier photocathode work of Henke, Knauer and Premaratne (1981)²⁷. The model will now be presented in brief.

The QE of CsI coated MCPs can be written as

$$QE_{MCP} = f(1 - e^{y(E)}) \quad (7)$$

Where $f = 0.58$ is the open area ratio of the MCPs and represents the maximum possible QE. $y(E)$ is the mean photo-electron yield of the photocathode as a function of energy. The QE is then the Poisson probability of producing a photo electron yield of one or greater given a mean yield of $y(E)$.

The yield, $y(E)$, written as

$$y(E) = \Lambda(E)\rho_{CsI}\mu(E)_{CsI} \quad (8)$$

is just the photo absorption within an electron range of the photocathode surface, where $\Lambda(E)$ is the electron range, $\mu(E)_{CsI}$ is the mass absorption coefficient of CsI and ρ_{CsI} is the mass density of CsI. The function $\Lambda(E)$ contains all the complex physics of electron transport of the photocathode. Furthermore, $\Lambda(E)$ is reported to vary only weakly as a function of energy (Henke, Knauer and Premaratne 1981).

From the above two equations one can solve explicitly for $\Lambda(E)$ as a function of the discretely measured MCP QE values QE_i .

$$\Lambda(E_i) = \frac{\ln(1 - \frac{QE_i}{f_{pore}})}{\mu(E)_i\rho} \quad (9)$$

A piece-wise spline interpolation was performed between the well behaved regions of the $\Lambda(E_i)$ points. The resulting MCP QE model was then determined by incorporating the $\Lambda(E)$ interpolation into Equations 8 and

7. The resulting MCP QE “model” depends on the Cs and I mass absorption coefficients (Henke 1993)²⁰ to determine jump ratios and photocathode edge locations. Comparing the interpolated MCP QE with synchrotron data showed that the interpolated jump ratios are too high and true edge locations are displaced to higher energies. This displacement of M edges of high Z materials has been observed elsewhere (Owens *et al.*, 1996)²⁸.

The second set of synchrotron data that spanned the Cs and I M edges was rescaled to match the flat field QE value at 525 eV by the use of an additive constant. This synchrotron data was then used to “replace” the interpolated data between 600 and 800 eV. The use of an additive constant was justified on account of higher order contamination in the synchrotron beam.

A list of synchrotron and XRCF QE values, corrected for normal incidence, and FF MCP QE values, that were input to the interpolation scheme is presented in Table 3.

HRC-I MCP QE			
Energy (eV)	MCP QE	Origin	Error
277	0.39/0.38	FF/XRCF	0.04
290	0.352	Synch	0.04
300	0.326	Synch	0.03
310	0.330	Synch	0.03
320	0.334	Synch	0.03
330	0.329	Synch	0.03
340	0.332	Synch	0.03
350	0.327	Synch	0.03
525	0.30	FF	0.03
851	0.41	FF	0.04
1487	0.34	FF	0.03
2560	0.166	XRCF	0.002
3500	0.126	XRCF	0.002
4510	0.093	XRCF	0.002
4600	0.120	XRCF	0.001
4800	0.117	XRCF	0.001
4900	0.128	XRCF	0.002
4960	0.127	XRCF	0.001
5060	0.149	XRCF	0.002
5130	0.145	XRCF	0.001
5250	0.152	XRCF	0.001
5320	0.152	XRCF	0.001
5480	0.159	XRCF	0.001
5660	0.157	XRCF	0.001
6300	0.156	XRCF	0.002
7000	0.148	XRCF	0.001
8000	0.153	XRCF	0.001
9000	0.168	XRCF	0.002

Table 3: Table of HRC-I QE values. All values except 8000 and 9000 eV were used in the QE interpolation. XRCF errors are purely statistical. FF and Synchrotron errors include 10% systematic contribution.

The overall interpolated QE of the HRC-I MCPs is presented in Figure 10.

3.2.6 In-Flight QE/EA Verification

The on axis EA of the HRC-I/HRMA is presented in Figure 11. It is the product of the above discussed subassembly calibration models.

The inflight verification of HRC-I Quantum Efficiency (QE) and Effective Area (EA) presents a challenging problem. Celestial X-ray sources have complex spectra and many of these sources are temporally variable. Furthermore, the HRC detectors have very limited ($\frac{\Delta E}{E} \sim 1$) energy resolution and can not independently determine the nature of the input spectrum.

Two techniques for inflight QE and EA verification will now be discussed. At present only one of these techniques has been implemented for the HRC-I. The two techniques are a broad band verification over an entire input spectrum and narrow band verification using either the LETG or HETG.

Narrow band verification has been performed successfully with the HRC-S detector and the results are presented elsewhere in these proceedings^{5,6}. In this narrow band technique, a well known source such as the white dwarf HZ43 is observed with the transmission gratings. The dispersed spectrum in conjunction with the mirror, grating, and source spectrum models allows one to make an in-flight measurement of QE. This measurement can then be used to verify the preflight model. Since the HRC-I is only considered as a backup grating readout, no such appropriate grating observations have yet been made.

The broad band technique relies on examining sources that are not temporally variable and for which a spectrum is known or can be determined. Ideal candidates are supernova remnants (SNRs) that have been observed with other instruments on the CXO (ACIS) or by other X-ray observatories. For the present analysis, we present results for Cassiopeia A and G21.5-09, two SNRs that have been observed during the calibration phase of the CXO mission with both the ACIS and the HRC-I detectors.

A region of the source image observed with ACIS is analyzed using the Chandra X-ray Science Center (CXC) spectral fitting tools (SHERPA)²⁹. Using a counts spectrum and the appropriate response matrices for the observation, an incident photon spectrum is determined. This photon spectrum is multiplied by the HRC-I effective area and integrated to determine a predicted rate. This predicted rate is then compared with the actual rate obtained from the identical region of the HRC-I observation. The technique and the results are pictorially presented in Figures 12 and 13; the plots show the ACIS counts spectra, the photon spectra and the measured and predicted rates. The results are remarkably close given the uncertainties in determining spectra. The larger discrepancy for Cas A is understandable given the size and the spatial and spectral complexity of the source. The HRC-I broad band effective area verification has also been compared with HRC-S observations of

Source	HRC-I predicted rate	HRC-I measured rate	HRC-S predicted rate	HRC-S measured rate
Cas A	10. <i>cts s</i> ⁻¹	9.3 <i>cts s</i> ⁻¹	8.9 <i>cts s</i> ⁻¹	8.2 <i>cts s</i> ⁻¹
G21.5-09	0.50 <i>cts s</i> ⁻¹	0.51 <i>cts s</i> ⁻¹	0.37 <i>cts s</i> ⁻¹	0.36 <i>cts s</i> ⁻¹

Table 4: Results of broad band EA verification. Comparison of predicted and measured rates of HRC-I and HRC-S.

the same two sources, G21.5-09 and Cassiopeia A. The results are presented in Table 4 and in (R. Kraft *et al.* 2000)⁵. The rates are in agreement with the respective HRC-I and HRC-S effective area models. This broad-band QE verification will be an ongoing process throughout the entire CXO mission as more HRC-I observations are made.

3.3 Point Spread Function (PSF)

Flight and preflight performance of the HRC-I detectors have indicated several minor imaging problems. The causes and cures for these problems will now be discussed. The present best HRC-I/HRMA PSF will then be presented and compared to preflight predictions.

The gain of the HRC-I MCPs has a high modal value and a large variance. Furthermore, the spatial dependence of detector gain varies over the HRC-I; it is centrally peaked. Due to the large gain of some events, primarily those in the center of the detector, there is evidence of amplifier saturation in the fine position charge values. This saturation occurs for $\sim 1\%$ of events and manifests itself as a secondary “ghost” image displaced $\approx 5.5\text{ mm}$ ($\approx 11\text{ arcsec}$) from the main image. These saturated events if not removed greatly complicate the instrument PSF. These saturated events are easily filtered without significantly affecting the detector efficiency.

An other imaging artifact is evident for events with a negative fine position, fp . This second feature is due to electronic ringing in the fine position circuitry induced by switching in the coarse position logic. The modified three-tap algorithm (“hyperbolic locus test”) as discussed in the section on event processing successfully removes this feature and the “ghost” with little loss of valid signal.

Two images of the the RS CVn star AR Lac are presented in Figure 15. The figures show the result of performing the hyperbolic locus test on the HRC-I events. It is clear that the secondary “ghost” image has been greatly reduced in the processed data. Analysis shows that the ghost is reduced from $\sim 1\%$ to $< 0.1\%$.

Figure 16 presents a comparison of the in flight HRC-I/HRMA PSF with HRMA ray-trace simulations at two energies. The ray trace simulations incorporate a $0.17''$ (rms) simulated aspect blur and an HRC instrumental blur of $0.15''$ (rms). The instrumental blur is from laboratory measurements. The combined HRC-I HRMA PSF shows that approximately 90% of the photons are contained within a $1.8''$ diameter circle and approximately 50% are contained within a $0.75''$ diameter circle.

4 CONCLUSIONS AND DISCUSSION

We have presented the most recent on axis effective area model for the HRC-I detector. This model has been tested and verified using in-flight observations. Results of these tests have shown that the HRC-I EA is consistent with preflight predictions. These techniques will form the basis of an on going program of HRC-I calibration verification and refinement which will continue throughout the Chandra mission. There is still uncertainty in the EA of the HRC-I detector for energies below 277 eV; Laboratory and in flight calibrations are being planned to remedy this.

Several methods of background reduction for the HRC-I detector have been presented. Using the on-board anti-coincidence shield and off-line event processing, the spatially averaged background for the HRC-I detector has been found to be $\approx 1 \times 10^{-5}\text{ cts s}^{-1}\text{ arcsec}^{-2}$. This background varies by $\sim 10\%$ across the HRC-I detector. These and other background reduction techniques will continue to be pursued. Background maps with much better statistics will be made in the near future.

Two minor imaging problems associated with the HRC-I instrument have been eliminated using off line processing with little change in detector efficiency. The resulting imaging performance of the HRC-I detector in combination with the HRMA has been shown to be have a PSF with approximately 90% of the photons contained in a $1.8''$ diameter circle and approximately 50% contained in a $0.75''$ diameter circle.

More detailed information and WWW links can be found at:

5 ACKNOWLEDGEMENTS

We are grateful for the support of Jack Gomes, John Polizzotti, Everett Johnston, Richard Goddard, Desi Hamvas Frank Rivera and Peter Warren. This work has been supported by NASA contract NAS8-38248 and NAS8-39073 .

6 REFERENCES

- [1] Weiskopf, M.C., O'Dell, S.L. and Elsner, R.F., "Advanced X-Ray Astrophysics Facility - AXAF an Overview", X-Ray and Extreme Ultraviolet Optics, R.B. Hoover and A.B.C Walker Jr., eds., Proc. SPIE **2515**, 1995.
- [2] Zombeck, M.V., "Advanced X-Ray Astrophysics Facility (AXAF)", Proceedings of the International School of Space Science Course on "X-Ray Astronomy", Aquila, Italy, 1996 CfA preprint 4003. Available at:

http://hea-www.harvard.edu/hrc_art/axaf_art/axaf_art1.html
- [3] Markert, T.H., Canizares, C.R., Dewey, D., McGuirk, M., Pak, C.S., Schattenburg, M.L., "High Energy Transmission Grating Spectrometer (HETGS) for AXAF", in *EUV, X-Ray, and Gamma-Ray Instrumentation for Astronomy V*, SPIE **2280**, (1994).
- [4] Brinkman, A.C., van Rooijen, J.J., Bleeker, J.A.M., Dijkstra, J.H., Heise, J., de Korte, P.A.J., Mewe, R., and Paerels, F., *Astro. Lett. and Commun.*, 26, 87 (1987).
- [5] Pease, D.O., *et. al.* SPIE **4012**, 20000.
- [6] Kraft, R.P., Chappell, J.H., Kenter, A.T., Meehan, G.R., Murray, S.S., Zombeck, M.V., Donnelly, R.H., Drake, J.J., Johnson, C.O., Juda, M., Patnaude, D., Pease, D.O., Ratzlaff, P.W., Wargelin, B.J. Zhao, P., Austin, G.K., Fraser, G.W., Pearson, J.F., Lees, J.E., Brunton, A.N., Barbera, M., Collura, A., Serio, S. "In-flight Performance and Calibration of the Chandra HRC-S Readout", SPIE **4012**, 2000.
- [7] Giacconi, R. *et al.*, *Astrophysical Journal*, 230, 1979.
- [8] Zombeck, M.V., David, L.P., Harnden, F.R. Jr. and Kearns, K., "Orbital Performance of the High Resolution Imager (HRI) on ROSAT", SPIE **2518**, (1995).
- [9] Kenter, A.T., Chappell, J.H., Kraft, R.P., Meehan, G.R., Murray, S.S., Zombeck, M.V., Fraser, G.W., "The High Resolution Camera on AXAF", Imaging Detector", SPIE **2808**, (1996).
- [10] Kraft, R.P., Chappell, J.H., Kenter, A.T., Kobayashi, K., Meehan, G.R., Murray, S.S., Zombeck, M.V., Smithsonian Astrophysical Observatory; Fraser, G.W., Pearson, J.F., Lees, J.E., Brunton, A.N., Pearce, S.E., University of Leicester (UK); Barbera, M., Collura, A., Serio, S., Istituto e Osservatorio Astronomico G.S. Vaiana (Italy) "Performance and Calibration of the AXAF High Resolution Camera II: Spectroscopic Detector", SPIE **3114**, (1997).
- [11] Kenter, A., Goddard, R., Gomes, J., Lessing, J., Murray, S., Moore, R., Roll, R., Valenza, M., Zombeck, M., "The MCP readout for the AXAF-I grating spectrometer", in *X-Ray Detector Physics and Applications II*, SPIE **2009**, 84, (1993).

- [12] Meehan, G.R., Chappell, J.H., Kenter, A.T., Kraft, R.P., Kobayashi, K., Murray, S.S., Zombeck, M.V., Barbera, M., Collura, A. "Measurement of the Transmission of the UV ion Shields of the AXAF High Resolution Camera", SPIE **2808**, (1996).
- [13] Meehan, G.R., Murray, S.S., Zombeck, M.V., Kraft, R.P., Kobayashi, K., Chappell, J.H., Kenter, A.T., Barbera, M., Collura, A., Serio, S., Istituto e Osservatorio Astronomico G.S. Vaiana (Italy) "Calibration of the UV/ion shields for the AXAF High Resolution Camera", SPIE **3114**, (1997).
- [14] Chappell, J.H., Martin, R.K., Murray, S.S. and Zombeck, M.V. "Background Reduction in Microchannel Plates", SPIE **1344**, 176, (1990).
- [15] Chappell, J.H. and Murray, S.S., "Position Modeling for the AXAF High Resolution Camera", SPIE **1159**, 460, (1989).
- [16] Kenter, A.T., Flanagan, K.A., Meehan, G.R., Murray, S.S., Zombeck, M.V., Fraser, G.W., Pearson, J.F., Lees, J.E., Brunton, A.N. and Pearce, S.E. "MCP selection for the HRC on AXAF" SPIE **2518**,1995.
- [17] Dietz, K.L., Elsner, R.F., Joy, M.K., O'dell, S.L., Ramsey, B.D., Weisskopf, M.C., Armstrong, A.W., Colborn, B.L., Kanvec, N. "Shielding Simulations for the Advanced X-Ray Astrophysics Facility" SPIE **2518** 1995
- [18] (Zombeck, M.V., Barbera, M., Collura, A. , and Murray, S.S., Ap. J. Lett., 487, L69, 1997).
- [19] Van Speybroeck, L.P "Performance Expectations versus Reality", SPIE **3113**,(1997).
- [20] Henke, B. L., Gullikson, E. M., and Davis, J. C., Atom. Data and Nucl. Data Tables, **54**(2), 181, JUL93.
- [21] Kolodziejczak, J.J., Austin, R.A., Elsner, R.F., Joy, M.K., Sulkanen, M., Kellogg, E.M. and Wargelin, B.J., "X-ray Source System at the MSFC X-ray Calibration Facility" Proc.,SPIE **2515**, (1995).
- [22] Patnaude, D. *et al.*, "Effective Area of the AXAF High Resolution Camera (HRC)", *EUV, X-Ray, and Gamma-Ray Instrumentation for Astronomy VIII*, O. H. W. Siegmund and M. A. Gummin, eds., Proc. SPIE 3445, 1998.
- [23] Kenter, A.T.,Meehan, G.R., "HRC QE versus Angle of Incidence", Internal SAO memorandum. September 24,1998. Available at :
http://hea-www.harvard.edu/HRC/calib/pore_ang.ps
- [24] Rideout, R. A. *et al.*, "Synchrotron Measurements of the Absolute X-ray Quantum Efficiency of CsI-coated Microchannel Plates", *EUV, X-Ray, and Gamma-Ray Instrumentation for Astronomy VIII*, O. H. W. Siegmund and M. A. Gummin, eds., Proc. SPIE 3445, 1998.
- [25] Pearce, S.E., Lees, J.E., Pearson, J.F., Fraser, G.W., Brunton, A.N., Flanagan, K.A., Kenter, A.T., Barbera,M.,Dhanak, V.,Robinson, A., Teehan,D. "Synchrotron calibration of Alkali Halide Coated Microchannel Plate Detectors in the 50-350 and 2000-6000 eV Bands", SPIE **2518**,1995.
- [26] Juda, M., "A Simple Model for the QE of CsI coated MCPs", SAO Internal Memo, 1997. Available at:
<http://hea-www.harvard.edu/~juda/memos/>
- [27] Henke, B. L.,Knauer, J.P.,Premaratne, K, "The characterization of X-ray photocathodes in the 0.1-10-keV photon energy region". Journal of Applied Physics, vol. 52, Mar. 1981, p. 1509-1520.
- [28] (Owens,A., Bayliss, S.C., Durham, P.J., Gurman, S.J. and Fraser, G.W., Ap.J.**468**,1996
- [29] 'CIAO Data Analysis'
<http://asc.harvard.edu/ciao/>
 and
<http://asc.harvard.edu/udocs/docs/docs.html>

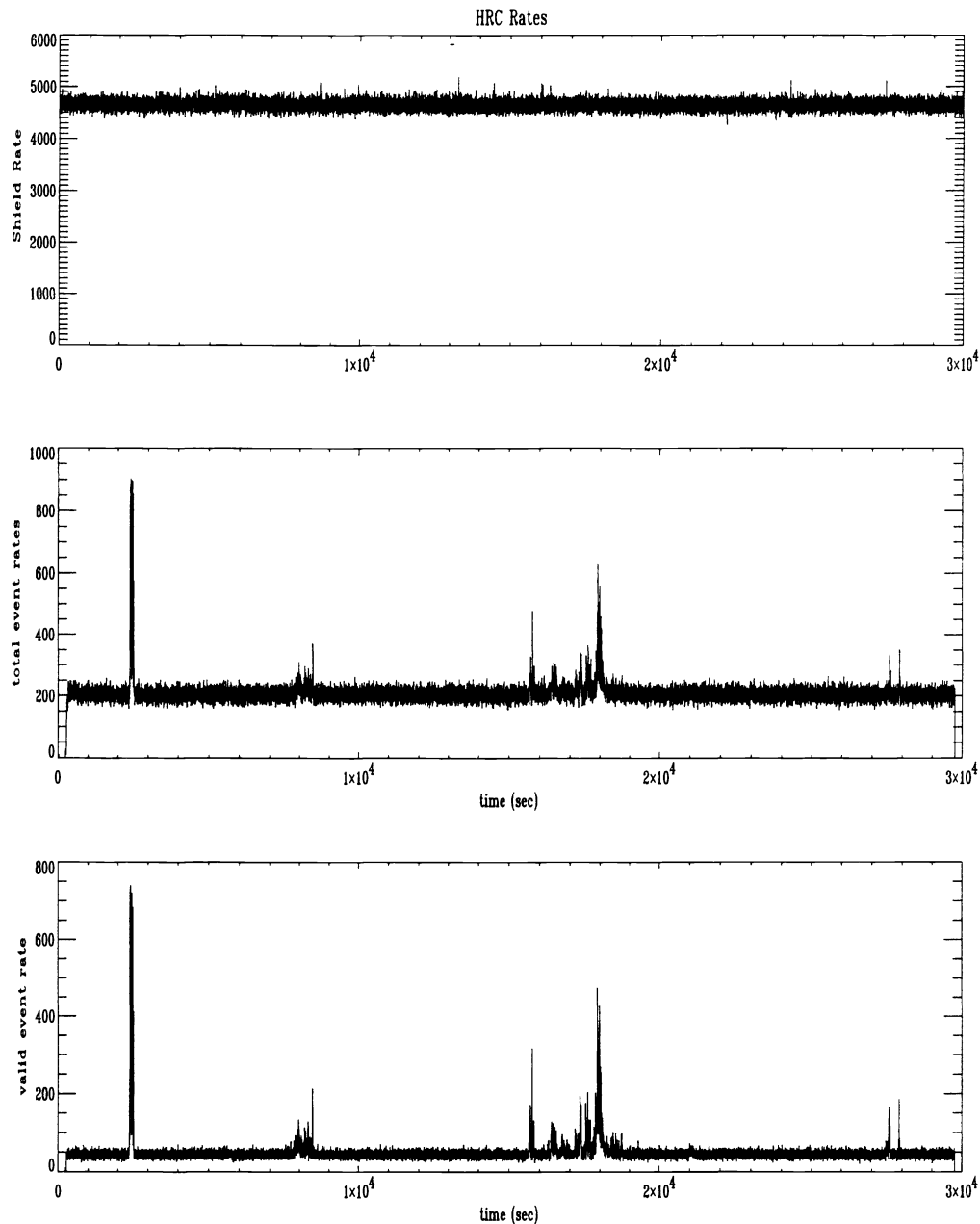


Figure 5: The background variability during a ~ 30 ksec HRC-I observation of the SNR G21.5-09 taken on 1999-10-25 at 04:52:25GMT. The total event rate and the valid event rate show correlated bursts up to ≈ 800 cts s^{-1} . These bursts in rate are not concentrated in any particular area but are uniformly distributed over the entire HRC-I detector. The anticoincidence shield shows no correlated enhancements; its rate is approximately constant at ~ 4500 cts s^{-1} . The total rate and the valid rate differ by ≈ 200 cts s^{-1} ; this difference is due primarily to vetoed cosmic ray events.

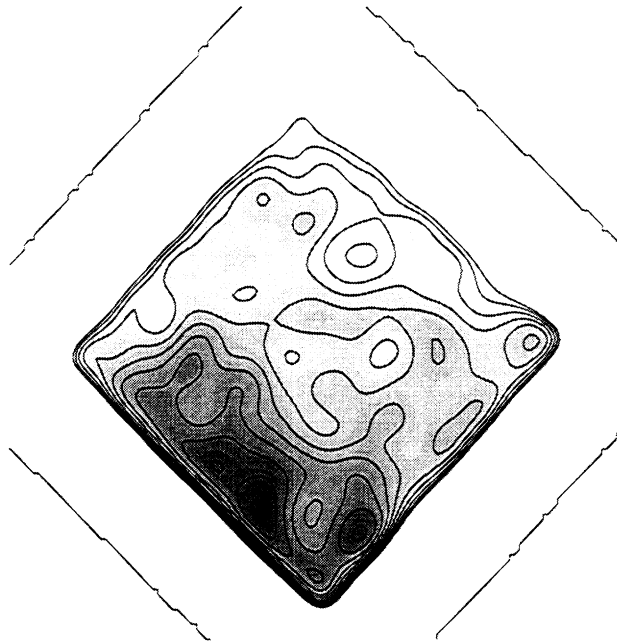


Figure 6: HRC-I Background Map. Average background is $\approx 1 \times 10^{-5} \text{ cts s}^{-1} \text{ arcsec}^{-2}$, with a $\sim 10\%$ gradient from top to bottom. The detector is oriented as in Figure 1. Smoothing is via wavelet decomposition. Contours are from 8.3 to $9.7 \times 10^{-6} \text{ cts s}^{-1} \text{ arcsec}^{-2}$.

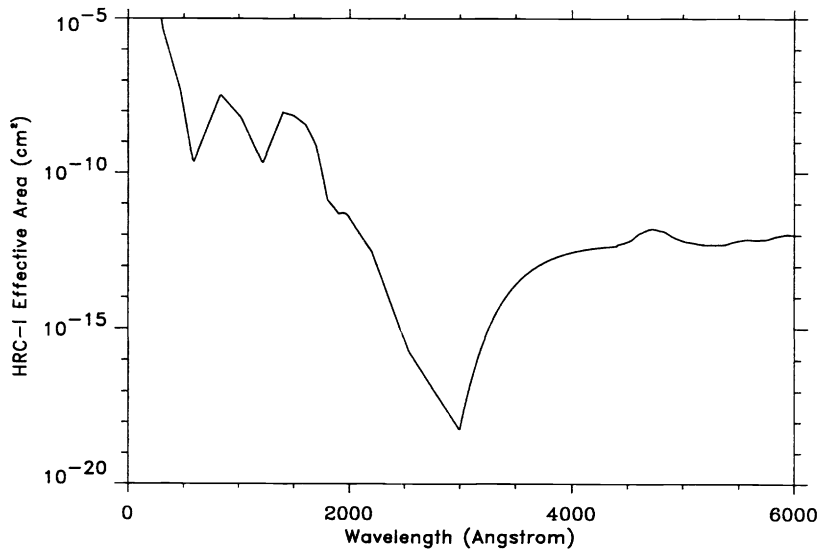


Figure 7: The HRC-I/HRMA Effective Area for out-of-band ultra-violet light.

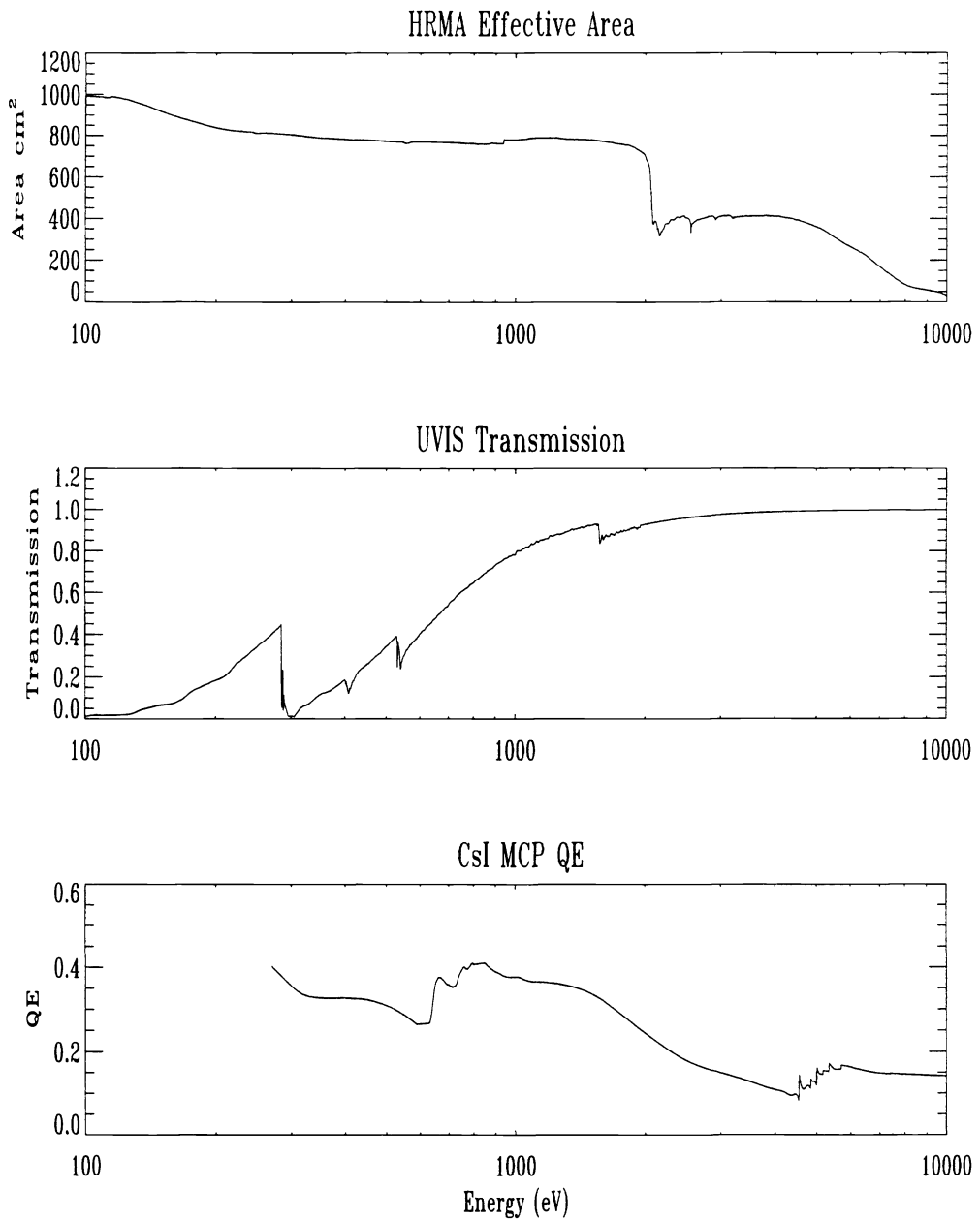


Figure 8: HRMA on axis Effective Area, HRC-I UVIS transmission and CsI coated MCP Quantum Efficiency. The MCP QE is not presented below 277eV due to inconsistencies in calibration data.

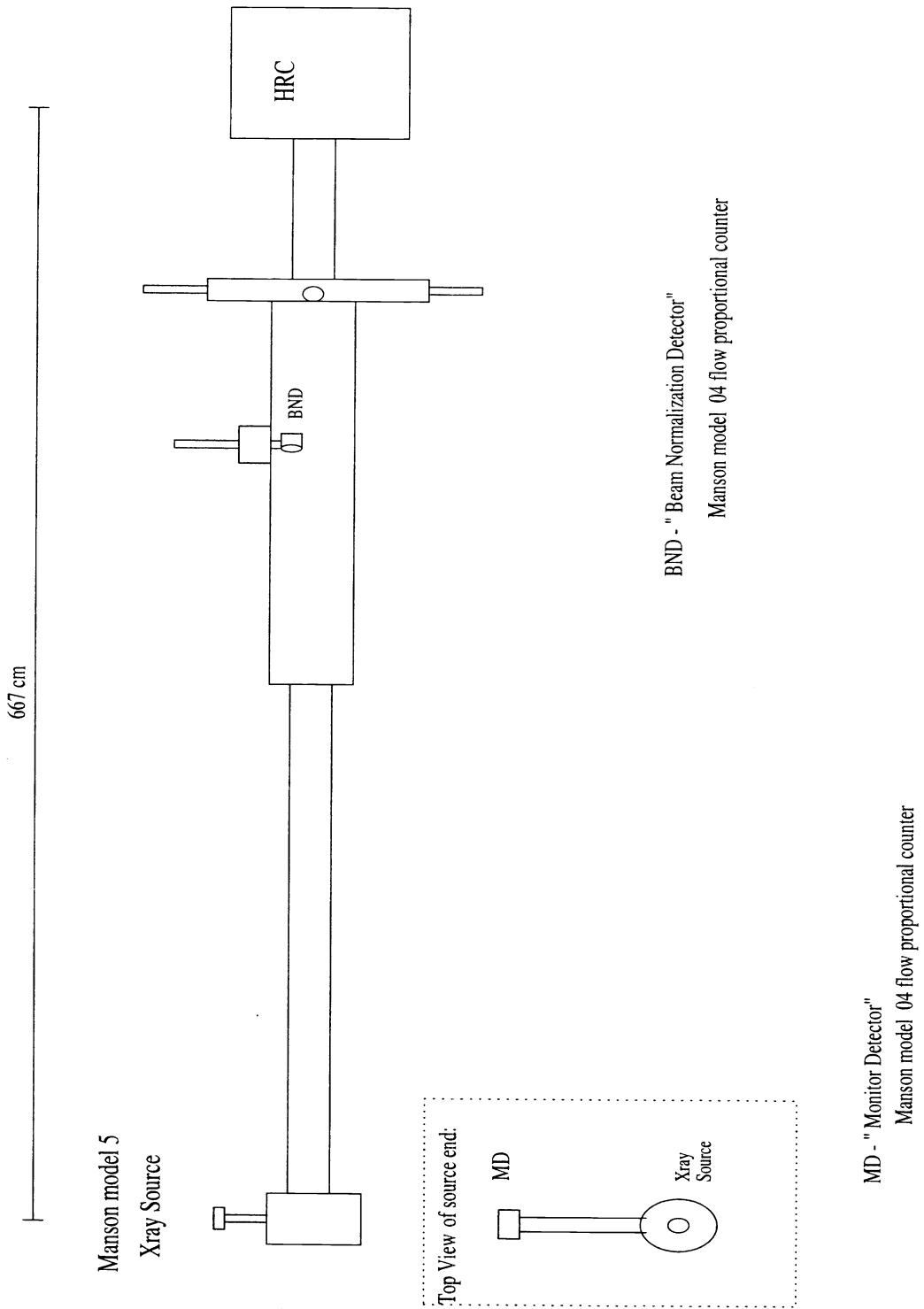


Figure 9: Facilities at the SAO HRC laboratory used for flat-field illumination of the HRC detectors.

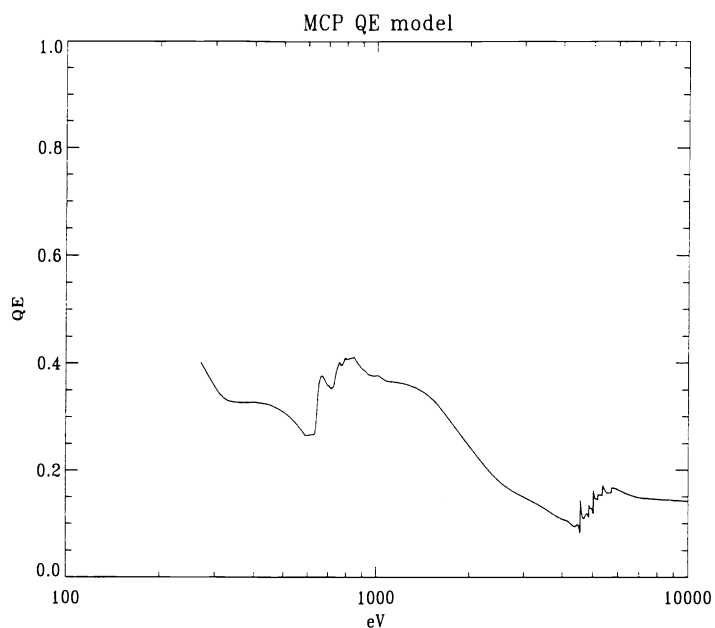


Figure 10: QE of CsI coated HRC-I MCPs. Data from XRCF, Flat field and synchrotron data were incorporated. No values below 277 eV are given due to inconsistencies in data.

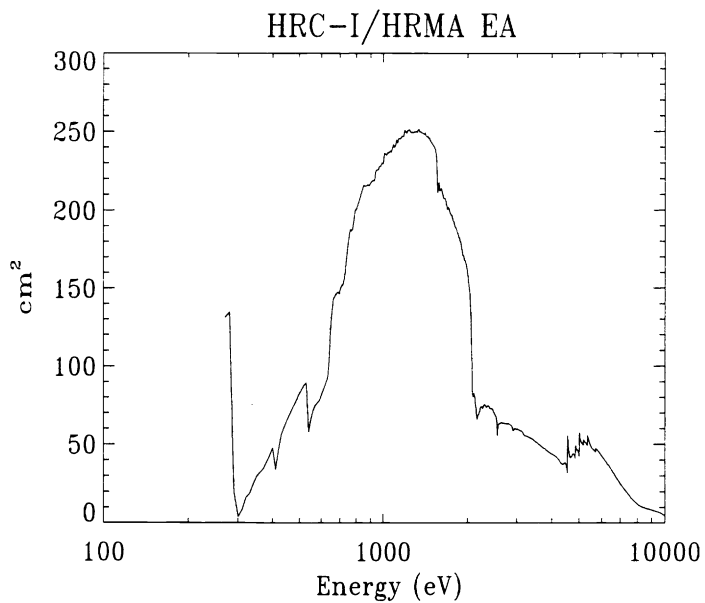
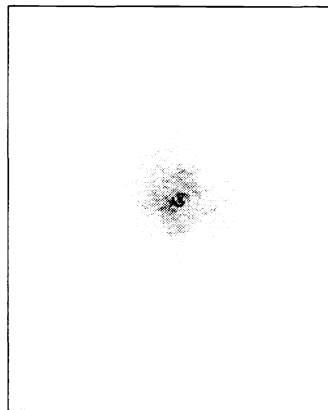
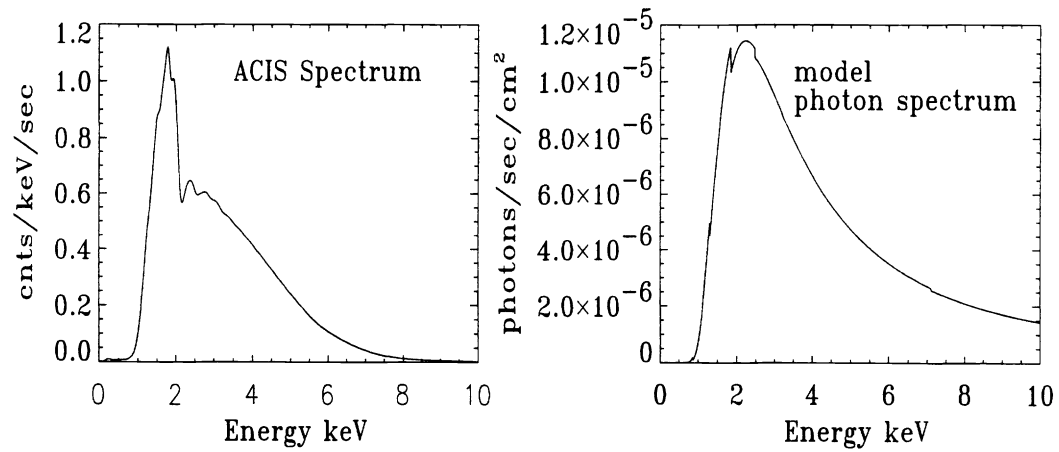


Figure 11: HRC-I/HRMA flight Effective Area .

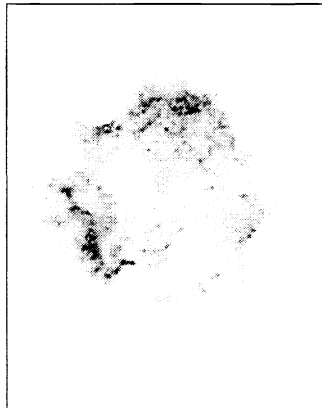
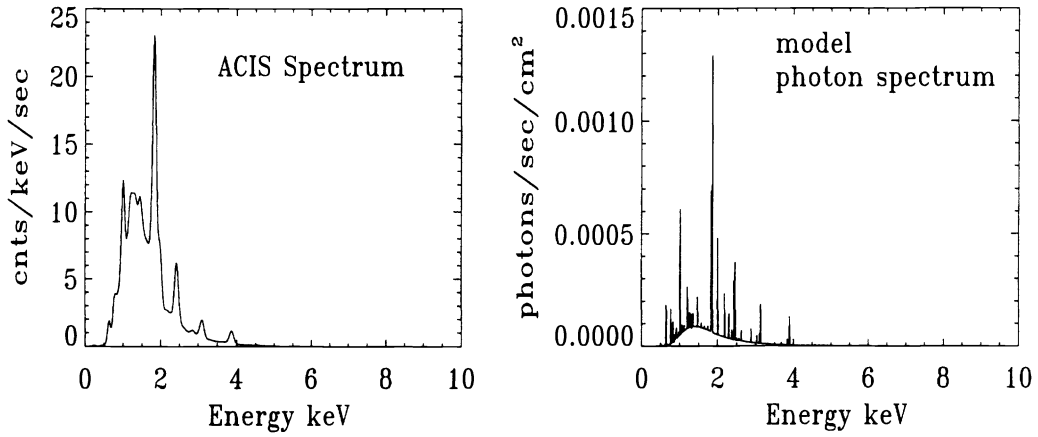


G21.5-09 (HRCI image)

Subregion predicted rate = 0.50 sec^{-1}

measured rate = 0.51 sec^{-1}

Figure 12: Pictorial representation of broad band verification of HRC-I Effective Area. Source is super nova remnant G21.5-09. HRC-I image is in lower left. A region of the source is analyzed with ACIS detector to determine counts spectrum. Using X-ray spectral modeling software a possible source spectrum is determined. Modeled spectrum is an absorbed power law. Spectrum is multiplied by HRC-I EA model and integrated. Results are within $< 2\%$ of predicted rate. Data has been corrected for background.



Cas-A (HRC-I image)

Subregion predicted rate = $10. \text{ sec}^{-1}$
 measured rate = 9.3 sec^{-1}

Figure 13: Pictorial representation of broad band verification of HRC-I Effective Area. Source is super nova remnant Cassiopeia A. HRC-I image is in lower left. A small region of the source is analyzed with ACIS detector to determine counts spectrum. Using X-ray spectral modeling software a possible source spectrum is determined. Modeled spectrum is an absorbed Raymond Smith plasma with variable abundances. Spectrum is multiplied by HRC-I EA model and integrated. Results are within $< 10\%$ of predicted rate. Data has been corrected for background.

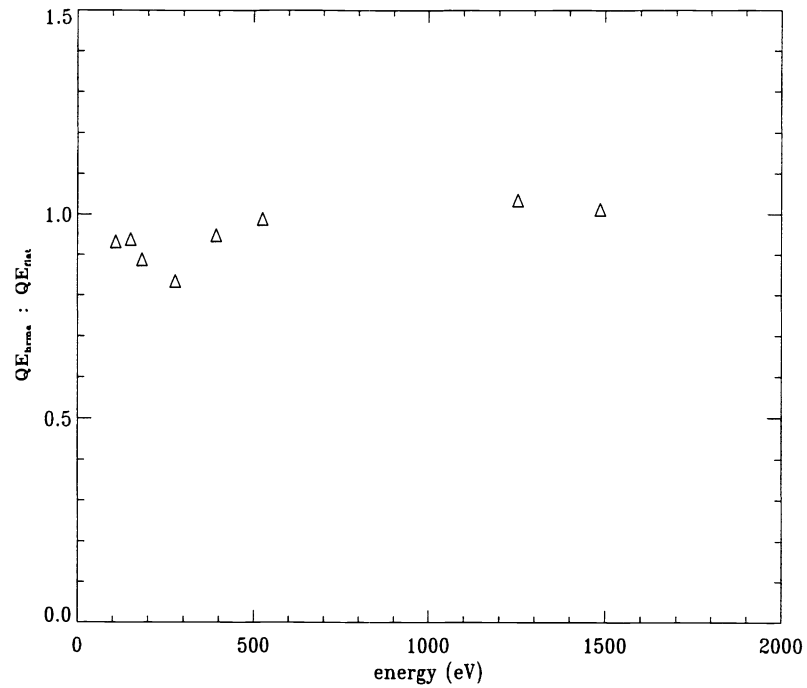


Figure 14: De-rating factors for applying HRC-I flat field data to operation in the converging beam of the HRMA. Derating factor was interpolated for other energies and was set = 1.0 for higher energies.

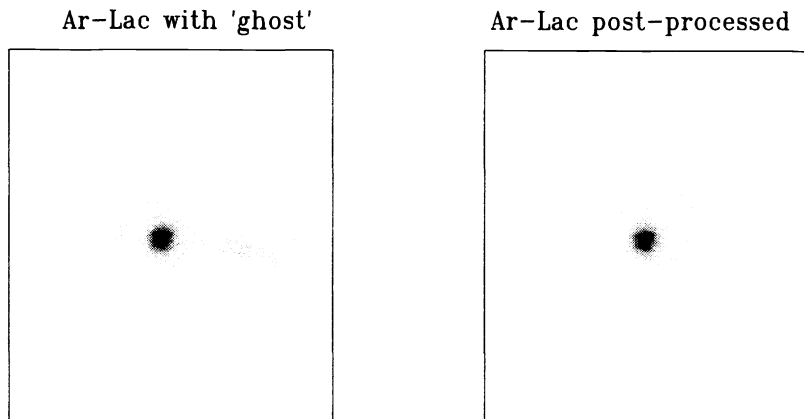


Figure 15: Results of modified 3-tap positioning algorithm (hyperbolic test) on the same RS CVn star AR Lac observation. Left image shows ghost image ~ 5.5 mm (11 arcsec) to the right (+v in detector coordinates) of main image. Intensity of “ghost” image is $< 1\%$. “Ghost” image is insignificant ($< 0.1\%$) in post processed data (right image).

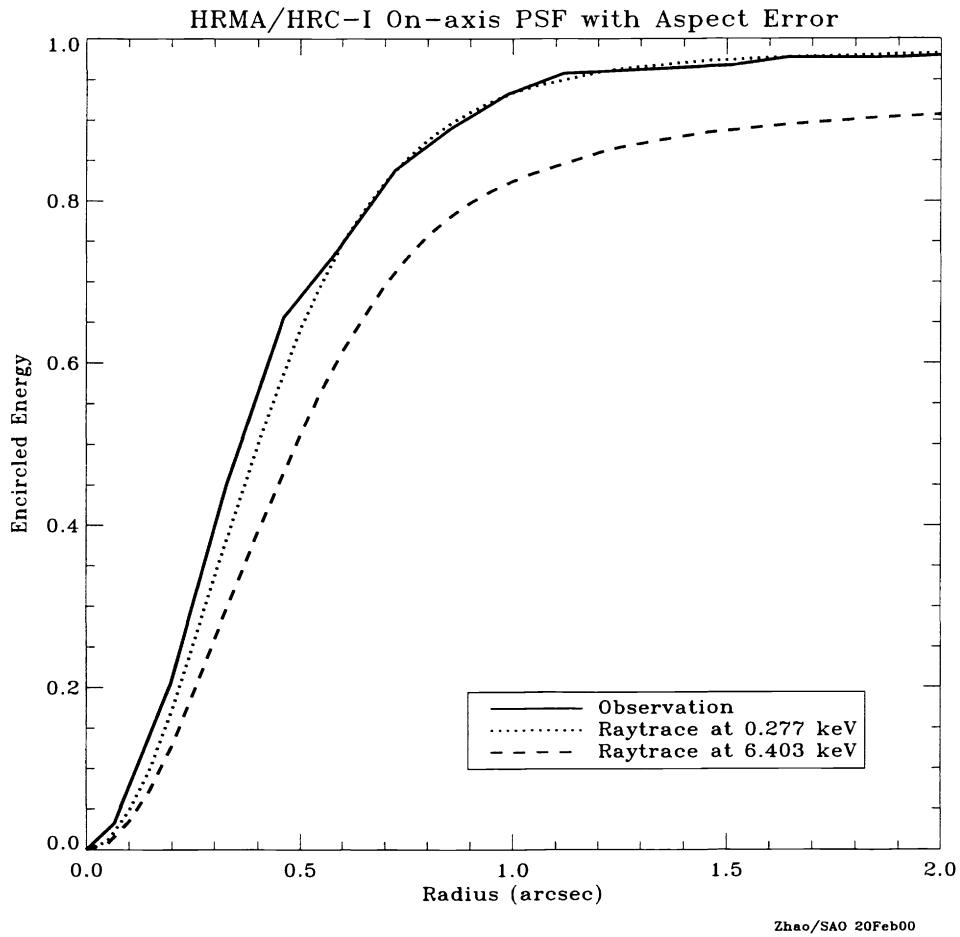


Figure 16: A comparison of the in flight HRC-I/HRMA PSF with HRMA ray-trace simulations. The ray trace simulations incorporate a $0.17''$ (rms) simulated aspect blur and an HRC instrumental blur of $\sim 0.16''$ (rms).